PHYSICAL REVIEW FLUIDS **3**, 124606 (2018)

Hierarchical random additive model for the spanwise and wall-normal velocities in wall-bounded flows at high Reynolds numbers

X. I. A. Yang,[1] R. Baidya,[2] Yu Lv,[3] and I. Marusic[2]
[1]*Mechanical and Nuclear Engineering, Penn State University, Pennsylvania 16801, USA*
[2]*Department of Mechanical Engineering, University of Melbourne, Melbourne, Victoria 3010, Australia*
[3]*Department of Aerospace Engineering, Mississippi State University, Mississippi 39759, USA*

(Received 11 June 2018; published 17 December 2018)

At high Reynolds numbers, the logarithmic range in wall-bounded flows spans many scales. An important conceptual modeling framework of the logarithmic range is Townsend's attached eddy hypothesis [*The Structure of Turbulent Shear Flow* (Cambridge University Press, Cambridge, 1976)], where high Reynolds number wall-bounded flows are modeled as assemblies of space-filling, self-similar, and wall-attached eddies. Recently, Yang *et al.* [Phys. Rev. Fluids **1**, 024402 (2016)] reinterpreted this hypothesis and developed the "hierarchical random additive process" model (HRAP), which provides further insights into the scaling implications of the attached eddies. For example, in a recent study [Yang *et al.*, Phys. Rev. Fluids **2**, 064602 (2017)], the HRAP model was used for making scaling predictions of the second-order structure function $\langle[u_i'(\mathbf{x}) - u_i'(\mathbf{x}')][u_j'(\mathbf{x}) - u_j'(\mathbf{x}')]\rangle$ in the logarithmic range, where u_i's are the velocity fluctuations in the ith Cartesian direction. Here, we provide empirical support for this HRAP model using high-fidelity experimental data of all three components of velocity in a high Reynolds number boundary layer flow. We show that the spanwise velocity fluctuation can be modeled as a random additive process, and that the wall-normal velocity fluctuation is dominated by the closest neighboring wall-attached eddy. By accounting for all the three velocities in all the three Cartesian directions, the HRAP model is formally a well rounded model for the momentum-carrying scales in wall-bounded flows at high Reynolds numbers.

DOI: 10.1103/PhysRevFluids.3.124606

I. INTRODUCTION

Wall-bounded flows are often encountered in engineering and geophysical applications. Near the wall, the flow is dominated by viscous effects, and away from the wall, the flow is subject to large-scale boundary effects. At high Reynolds numbers (Reynolds numbers that are relevant for aerodynamics and geophysics), a logarithmic range emerges between viscosity-dominated near-wall scales and the bulk-range scales [1,2]. Many efforts have been devoted to modeling the flow within the logarithmic range (see, e.g., Refs. [3–6]), and an important modeling framework is provided by the attached-eddy hypothesis. The attached-eddy model was pioneered by Townsend [7] and then extended by Perry, Chong, Marusic, and coauthors by accounting for wake effects, vortex clustering, and spatial exclusion of the wall-attached eddies of the same size [3,8–11]. A comprehensive review of the works as related to the hypothesis may be found in Ref. [12]. Briefly, the attached-eddy hypothesis models the high Reynolds number boundary layer flows as assemblies of space-filling, self-similar, and wall-attached eddies (see a sketch of the modeled boundary-layer flow in Fig. 1); and velocity fluctuations at a generic location in the flow field are modeled by adding up the eddy-induced velocities there. Earlier works as related to the attached-eddy idea have mostly relied on a few specifically-shaped eddies (e.g., Λ-eddy, Ω-eddy, etc. [9,10]), and there was only limited discussion on the scaling implications of the attached eddies. Recent works by Meneveau, Marusic,

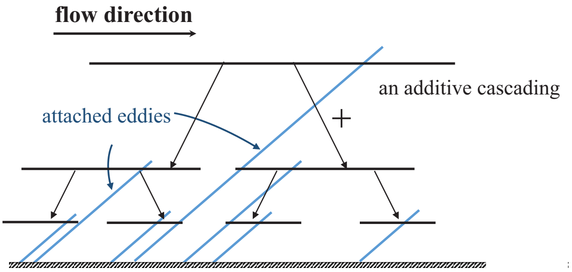

FIG. 1. A sketch of the modeled turbulent boundary layers at high Reynolds numbers. Three hierarchies of attached eddies (inclined solid lines) are sketched. The number of visible eddies on a vertical cut (as is sketched here) doubles as the sizes of the eddies halve. The velocity fluctuation at a generic point in the flow field is an additive superposition of the eddy-induced velocities.

Lohse, and coauthors have led to new insights into the scaling implications of the attached eddies [5,6,13,14], and one notable development was the "hierarchical random additive process" model (HRAP), where the eddy-induced velocities are modeled as random addends:

$$u = \sum_{i=1}^{N_z} a_i, \tag{1}$$

where i is an integer, and a_i's are addends that model the eddy-induced velocities at the wall-normal height z. Frisch referred to multifractal models as "hierarchical intermittency models" [15], where the term hierarchical refers to a collection of scales. The term "hierarhical" was also used to refer to "relative importance of entities within a group" in Ref. [16]. The term "hierarchical" in "hierarchical random additive process" refers to a collection of scales, and there is no relative importance between the scales. Throughout the paper, we will use u, v, and w for the streamwise (x), spanwise (y), and wall-normal (z) velocity fluctuations, respectively. The number of contributing eddies can be computed by integrating the eddy population density $P(z)$ from z to the boundary-layer height,

$$N_z = \int_z^\delta P(z')dz' \sim \log(\delta/z), \tag{2}$$

where the eddy population density $P(z) \sim 1/z$ is inversely proportional to the wall-normal distance (see Fig. 1). This compact form proves to be quite useful. For example, it directly follows from Eq. (1) that

$$\langle u^2 \rangle = \left(\sum_{i=1}^{N_z} a_i \right)^2 = N_z \langle a^2 \rangle \sim \log(\delta/z), \tag{3}$$

i.e., the logarithmic scaling of $\langle u^2 \rangle$ as a function of the wall-normal distance, where $\langle \cdot \rangle$ is the ensemble average of the bracketed quantity, δ is the boundary layer height, a_i's are identically, independently distributed random addends (i.i.d., $\langle a_i a_j \rangle = 0$ for $i \neq j$, and a is a random variable that has the same statistical properties as a_i). Determining the constants in Eq. (3), i.e., the slope and the intercept of the logarithmic scaling, requires knowledge of the statistical properties of the addends a_i. However, this is not straightforward, as it is difficult, if not impossible, to extract an attached eddy from a turbulent flow field. Nonetheless, we will demonstrate that by assuming the addends to follow a Gaussian behavior and quantifying deviations from the resulting Gaussian statistics, a new physical insight of the wall-bounded flow can be obtained.

Unless otherwise noted, we will use the wall units, i.e., the friction velocity u_τ and the viscous length scale ν/u_τ, for normalization. The HRAP model has been used to provide scaling estimates for velocity moment-generating-functions [17] and velocity structure functions [18], and quantities that involve the wall-shear stress fluctuations and fluctuations of passive scalars [19] in wall-bounded flows at high Reynolds numbers. However, so far, the model is formally only for the streamwise velocity fluctuation.

Due to the experimental challenges associated with accurately measuring the weaker spanwise and wall-normal fluctuations compared to the streamwise counterpart in a wall turbulent flow, traditionally the focus of near-wall turbulence modeling has been on the u velocity. However, advancements in computational capabilities and measurement techniques over the past two decades have led to renewed interest in the spanwise and wall-normal velocity components. For example, del Alamo *et al.* [20] found evidence of wall-scaling in two-dimensional spectra for all three velocity components. Furthermore, Krug *et al.* [21] showed universality across a wide range of flows for the streamwise and spanwise velocities using an extended form (i.e., the ratio between two structure functions of different orders). Access to three-dimensional volume in direct numerical simulation (DNS) allows two-point statistics to be constructed, which captures the bulk contribution to the u, v, and w velocities from features that remain coherent in the order of δ [22]. As the two-point statistics are obtained by ensembling in time, they are symmetric in the homogeneous direction. However, Sillero *et al.* [22] found that instantaneously the area occupied by the positive and negative spanwise velocities in a wall-parallel plane from a channel DNS have tendency to be oblique and inclined at $\pm 45^\circ$ to the flow direction in the wake region. Since the likelihood of negative or positive spanwise velocity is equal, this leads to a squarish-shaped two-point correlation function. Furthermore, de Silva *et al.* [23] found that the obliqueness of spanwise velocity extend into the log region if conditioned both on the sign of the streamwise and spanwise velocities, based on wall-parallel large field of view particle image velocimetry (PIV) experiments in turbulent boundary layers. Motivated by these new insights gained in the spanwise and wall-normal components, here we aim to extend the work of Yang *et al.* [6] to include these velocity components.

The rest of the paper is organized as follows. In Sec. II, we detail the model formalism for the spanwise and the wall-normal velocity fluctuations. The model is tested in Sec. III, and conclusions are given in Sec. IV. We use the cross-wire measurements of boundary layer flow at $\mathrm{Re}_\tau \approx 10\,000$ for testing the model. Details of the dataset can be found in Refs. [24,25].

II. A HRAP MODEL FOR THE SPANWISE AND WALL-NORMAL VELOCITY FLUCTUATIONS

Following Ref. [18], the spanwise velocity fluctuation at a wall-normal height z is modeled as

$$v = \sum_{i=1}^{N_z} b_i, \tag{4}$$

where b_i are i.i.d. addends [but possibly with a different distribution than the a_i's in Eq. (1)]. For now, we make the simplification that b_i and a_i are independently distributed. Because of the wall blocking effect, the wall-normal fluctuation is dictated by the closest neighboring attached eddy

$$w = -C_w a_{N_z}, \tag{5}$$

where a_{N_z} is the last additive in Eq. (1), and C_w is a positive constant. A formal discussion of the locality of the wall-normal velocity fluctuation may be found in, e.g., Refs. [3,7]. Here, we only briefly recap the basic ideas in Refs. [3,7]. Consider, for example, two wall-attached eddies that are very different in their sizes. Figure 2 shows a sketch of such two wall-attached eddies. Let h_B and h_A be the heights of eddy-B and eddy-A, and let $h_A \gg h_B$. The sum of the induced velocities in the wall-normal direction by eddy-A and its mirror at height h (denoted by a dot in Fig. 2) is approximately 0 because $h/(h_A - h) \approx h/(h_A + h) \approx 1$. (Note that in Ref. [7] prescription of a no-penetration, slip surface with $w(0) = 0$ is equivalent to a mirrored eddy.) However, the sum of the induced velocities by eddy-B and its mirror at the h is finite, because $h/(h_B - h) \neq h_B/(h_B + h)$. Hence, the local eddy determines the wall-normal velocity fluctuation. In addition to above

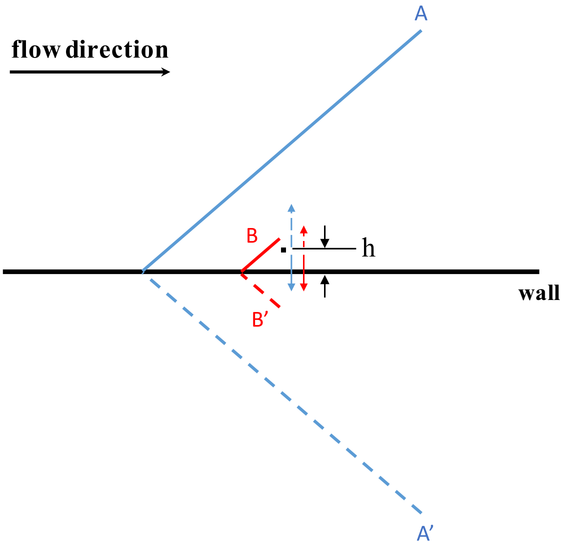

FIG. 2. A sketch of two wall-attached eddies eddy-A and eddy-B (solid lines), along with their mirror eddies, eddy A' and eddy B' (dashed lines). The induced velocity of a wall-attached eddy in a generic location in the flow is a sum of the induced velocity of this eddy and its mirror. The induced velocities at the dotted location at height h are indicated using arrows with the line types and colors in accordance with these of the sketched eddies.

arguments, Eqs. (1) and (5) lead to

$$\langle uw\rangle \sim -\sum_{i=1}^{N_z}\langle a_i a_{N_z}\rangle = -\langle a_{N_z} a_{N_z}\rangle = -\text{Const}, \tag{6}$$

i.e., the expected constant momentum flux in the logarithmic range.

The goal of this work is to provide empirical support for Eqs. (4) and (5). However, because neither of the equations can be directly verified, we will use Eqs. (4) and (5) to make scaling estimates of various statistics and compare these scalings to the experimental data. From a statistical perspective, central moments are useful tools for describing a stochastic quantity. High-order moments emphasize large fluctuations, and the general behaviors are characterized by low-order moments. However, central moments do not distinguish between positive and negative fluctuations, and a complete statistical characterization of the turbulent velocities is provided by the moment generating functions (MGFs), i.e., $\langle \exp(qv)\rangle$ and $\langle \exp(q_1 v(x) + q_2 v(x+r))\rangle$ if two-point flow statistics are of interest. The MGFs, by definition, can be used to compute central moments to arbitrary order

$$\langle v^m\rangle = \left.\frac{\partial^m \langle \exp(qv)\rangle}{\partial q^m}\right|_{q=0},$$

$$\langle v^m(x+r)v^n(x)\rangle = \left.\frac{\partial^m}{\partial q_1^m}\frac{\partial^n}{\partial q_2^n}\langle \exp[q_1 v(x) + q_2 v(x+r)]\rangle\right|_{q_1=0,q_2=0},$$

where m, n are integers. The parameters q, q_1, and q_2 may be used to as dials to emphasize different parts of the velocity probability density function (p.d.f.), e.g., a positive q emphasizes large positive v fluctuations and a negative q emphasizes negative v fluctuations. For example, a sketch of the premultiplied p.d.f. $\exp(qg)\cdot P(g)$ is shown in Fig. 3, where g is Gaussian and $P(g) \sim \exp(-g^2)$. Different parts of the g-p.d.f. are emphasized when choosing different q's, and a

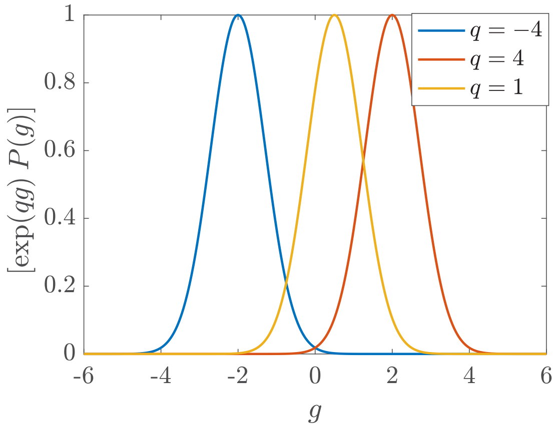

FIG. 3. Premultiplied p.d.f. of $\exp(qg)\cdot P(g)$ for g being a zero-mean unit-variance Gaussian variable. The premultiplied p.d.f.'s are normalized for better visualization. $\langle\exp(qg)\rangle$ equals the area under the corresponding premultiplied p.d.f.

large $|q|$ emphasizes the tail of the p.d.f. It is also worth noting that the MGFs as defined correspond to a highly simplified and real-valued subset of the more general object described by the Hopf equation [26], which is an equation of the generalized MGF, $\langle\exp(i\int\theta(\mathbf{x})\mathbf{u}(\mathbf{x})\mathbf{dx^3})\rangle$. The Hopf equation describes the full N-point joint p.d.f. of velocity fluctuations, where N is the total number of different spatial points needed for a complete description of the flow. The interest in the Hopf equation comes from the fact that it is linear, and therefore self-contained, requiring no closure [27]. Considering the usefulness of MGFs, our discussion will focus on the scalings of MGFs. We will make scaling estimates of velocity MGFs, and test the model's predicted scalings against the available experimental data.

Following the same arguments that lead to the power-law scaling of the streamwise MGFs [17,28], i.e.,

$$\langle\exp(q_u u)\rangle\sim(\delta/z)^{\tau_u(q_u)},\quad \tau_u(q_u)\sim\log[\langle\exp(q_u a)\rangle],\tag{7}$$

Eq. (4) leads to

$$\langle\exp(qv)\rangle=\langle\exp(qb)\rangle^{N_z}\sim(\delta/z)^{\tau_v(q)},\tag{8}$$

where the power-law exponent is

$$\tau_v(q)\sim\log[\langle\exp(qb)\rangle],\tag{9}$$

and b is a random addend that is statistically similar to the b_i's in Eq. (4). If the random addends b_i are Gaussian $\langle\exp(qb)\rangle\sim\exp(q^2)$ [29], Eq. (9) leads to

$$\tau_v(q)=Cq^2,\tag{10}$$

where C is a constant. Equations (8) and (10) may be used to compute the central moments of v,

$$\langle v^{2p}\rangle^{1/p}=\left[\left.\frac{\partial^{2p}\langle\exp(qv)\rangle}{\partial q^{2p}}\right|_{q=0}\right]^{1/p}\sim[(2p-1)!!]^{1/p}A_{1,v}\log\left(\frac{\delta}{z}\right),\tag{11}$$

leading to a logarithmic scaling of the even-order moment $\langle v^{2p}\rangle^{1/p}$, where

$$A_{1,v}=\left.\frac{d^2}{dq^2}[Cq^2]\right|_{q=0}=2C.\tag{12}$$

It is worth noting that the logarithmic scaling of $\langle v^2\rangle$ [i.e., taking $p = 1$ in Eq. (11)] was previously reported in, e.g., Refs. [30–32].

Gaussianality is but a crude approximation of real turbulence, and therefore the resulting Eq. (10) is also a crude approximation of the power-law exponent $\tau_v(q)$. If we do not invoke the Gaussian assumption, per the definition of $\tau_v(q)$, we know that $\tau_v(0) = 0$ because $\langle \exp(0 \cdot v)\rangle = 1$, and that $d^{2k+1}\tau_v/dq^{2k+1}|_{q=0} = 0$, because $\langle v^{2k+1}\rangle = 0$. Here $k = 0, 1, 2$, etc., is an integer. Using only the above two pieces of information, the central moments are

$$\begin{aligned}\langle v^2\rangle &= A_{1,v}\log(\delta/z)\\ \langle v^4\rangle &= 3A_{1,v}^2[\log(\delta/z)]^2 + \tau_v^{(4)}(0)\log(\delta/z)\\ \langle v^6\rangle &= 15A_{1,v}^3[\log(\delta/z)]^3 + 15\tau_v^{(2)}(0)\tau_v^{(4)}(0)[\log(\delta/z)]^2 + \tau_v^{(6)}(0)\log(\delta/z),\end{aligned} \tag{13}$$

where $\tau_v^{(k)}(0)$ is the kth derivative of $\tau_v(q)$ evaluated at $q = 0$, and $A_{1,v} = \tau_v^{(2)}(0)$. At sufficiently high Reynolds numbers and for $z \ll \delta$, the first term dominates and Eq. (13) degenerates to Eq. (11). Hence, as far as the central moments are concerned, invoking the Gaussianality or not leads to the same scaling predictions.

Evaluating two-point MGFs is slightly more involved than single-point MGFs. However, if we follow the steps in Ref. [17], for relevant two-point displacement r in the streamwise direction (i.e., $h = r\tan(\theta)$ being in the logarithmic range, where θ is the inclination angle of a typical wall-attached eddy), the two-point MGF is

$$W_v(q_1, q_2; z, r) \equiv \langle \exp(q_1 v(x) + q_2 v(x + r))\rangle \sim (z/\delta)^{-\tau_v(q_1)-\tau_v(q_2)}(r/\delta)^{\Phi_v(q_1,q_2)}, \tag{14}$$

where

$$\Phi_v(q_1, q_2) = \min[\tau_v(q_1) + \tau_v(q_2) - \tau_v(q_1 + q_2), 1]. \tag{15}$$

It follows from Eq. (14) that

$$W_v(q, -q; z, r) \sim (r/\delta)^{\min[\tau_v(q)+\tau_v(-q),1]}, \tag{16}$$

i.e., a scaling transition at $\tau_v(q) + \tau_v(-q) = 1$. Equations (10), (14), and (15) may be used to compute any two-point central moments. For example,

$$\begin{aligned}\langle v(x + r)v(x)\rangle &= \frac{\partial}{\partial q_1}\frac{\partial}{\partial q_2}W(q_1, q_2; z, r)\bigg|_{q_1=0,q_2=0} = \frac{\partial}{\partial q_1}\frac{\partial}{\partial q_2}(r/\delta)^{-2Cq_1q_2}\bigg|_{q_1=0,q_2=0}\\ &= A_{1,v}\log(\delta/r).\end{aligned} \tag{17}$$

The scaling transition is not relevant for deriving the central moments because q_1, q_2 are evaluated at $q_1 = 0$, $q_2 = 0$, and at $q_1 = 0$, $q_2 = 0$, we have $\Phi_v(q_1, q_2) < 1$. It then follows that

$$\langle (v(x) - v(x + r))^2\rangle = 2\langle v^2\rangle - 2\langle v(x)v(x + r)\rangle = 2A_{1,v}\log(\delta/z) - 2A_{1,v}\log(\delta/r) \sim \log(r/z). \tag{18}$$

Generally, the two-point MGFs can be used to compute $\langle v^m(x + r)v^n(x)\rangle$ for arbitrary m and n. With $\langle v^m(x + r)v^n(x)\rangle$ known, the even-order structure functions are known according to

$$\langle [v(x + r) - v(x)]^{2p}\rangle^{1/p} = \left[\sum_{n=1}^{2p} C_{2p}^n\langle v^n(x + r)v^{2p-n}(x)\rangle\right]^{1/p}, \tag{19}$$

and one may verify that

$$\langle [v(x + r) - v(x)]^{2p}\rangle^{1/p} \sim \log(r/z), \tag{20}$$

where $C_{2p}^{n} = 2p!/[(2p-n)!n!]$, and second that

$$S_{1,v} = \langle v(x)v(x+r)\rangle \sim \log(\delta/r), \tag{21a}$$

$$S_{2,v} = \left[\tfrac{3}{2}\langle v^2(x)v^2(x+r)\rangle - \tfrac{1}{2}\langle v^4(x)\rangle\right]^{1/2} \sim \log(\delta/r), \tag{21b}$$

$$S_{3,v} = \left[\tfrac{5}{2}\langle v^3(x)v^3(x+r)\rangle - \tfrac{3}{4}(\langle v(x)v^5(x+r)\rangle + \langle v^5(x)v(x+r)\rangle)\right]^{1/3} \sim \log(\delta/r). \tag{21c}$$

The same scalings in Eqs. (20) and (21) were reported for the streamwise velocity counterpart in Ref. [6], although a slightly different approach was taken in Ref. [6] for deriving these scalings.

In addition to the spanwise velocity MGFs, Eqs. (1), (4), and (5) give rises to power-law scalings of mixed MGF:

$$\begin{aligned}\langle\exp(q_u u + q_w w)\rangle &= \left\langle \exp\left(q_u \sum_{i=1}^{N_z} a_i + q_w(-a_{N_z})\right)\right\rangle = \left\langle \exp\left(q_u \sum_{i=1}^{N_z-1} a_i + (q_u - q_w)a_{N_z}\right)\right\rangle \\ &= \left\langle \exp\left(q_u \sum_{i=1}^{N_z-1} a_i\right)\right\rangle \left\langle \exp\left((q_u - q_w)a_{N_z}\right)\right\rangle \\ &= \langle\exp(q_u a)\rangle^{N_z-1} \cdot \langle\exp((q_u - q_w)a)\rangle.\end{aligned} \tag{22}$$

Next we will need to relate $N_z - 1$ to a wall normal distance, where 1 is an infinitesimal increment. For simplicity, the random additive model uses a discretized representation of the wall normal coordinate, which works well in most circumstances. However, in reality the hierarchies have a continuous distribution and hence $N_z - 1$ in discrete representation can be replaced by an analogous term $\log(\delta/(z+dz))$, where dz is an infinitestial increment. It then follows from the above equation that

$$\begin{aligned}\langle\exp(q_u u + q_w w)\rangle &\sim C_e[(z+dz)/\delta]^{-\tau_u(q_u)}\langle\exp(q_u a - q_w a)\rangle \\ &\sim C_e(z/\delta)^{-\tau_u(q_u)}(1+dz/z)^{-\tau_u(q_u)}\langle\exp(q_u a - q_w a)\rangle \\ &\sim C_e(z/\delta)^{-\tau_u(q_u)}[1-\tau_u(q_u)dz/z]\langle\exp(q_u a - q_w a)\rangle \\ &\sim C_e(z/\delta)^{-\tau_u(q_u)}\langle\exp(q_u a - q_w a)\rangle,\end{aligned} \tag{23}$$

where C_d, C_e are O(1) constants, $\tau_u(q)$ is the power-law scaling exponent of $\langle\exp(qu)\rangle$. The statistical object $\langle\exp(q_u u + q_w w)\rangle$ provides a new perspective for conducting quadrant analysis. We can emphasize different combinations of u and w by choosing different values for q_u and q_w, e.g., a positive q_u and a negative q_w emphasize events when u and w are positive and negative, respectively. The measured mixed MGFs may be compared to the model, i.e., Eq. (22), which function is determined using only measurements of the streamwise velocity. Measuring the combined p.d.f. of u and w, i.e., conducting conventional quadrant analysis, however, needs simultaneous measurements of both u and w. Last, in addition to $\langle\exp(q_u u + q_w w)\rangle$, the other quantity of interest include $\mathscr{W}(q_u, q_w; z) = \langle\exp(q_u u + q_w w)\rangle/\langle\exp(q_u u)\rangle$. Because the wall-normal velocity fluctuation is determined by the local attached eddy, and is statistically correlated to only the last addend in u, we may expect that $\langle\exp(q_u u + q_w w)\rangle \approx \langle\exp(q_u u)\rangle$. It follows from Eqs. (7) and (22) that

$$\begin{aligned}\mathscr{W}(q_u, q_w; z) = \langle\exp(q_u u + q_w w)\rangle/\langle\exp(q_u u)\rangle &\sim \frac{(z/\delta)^{-\tau_u(q_u)}\langle\exp(q_u a - q_w a)\rangle}{(z/\delta)^{-\tau_u(q_u)}} \\ &= \langle\exp(q_u a - q_w a)\rangle = \exp(C_u(q_u - q_w)^2),\end{aligned} \tag{24}$$

is independent of the wall-normal distance, where we assume the addend a is Gaussian.

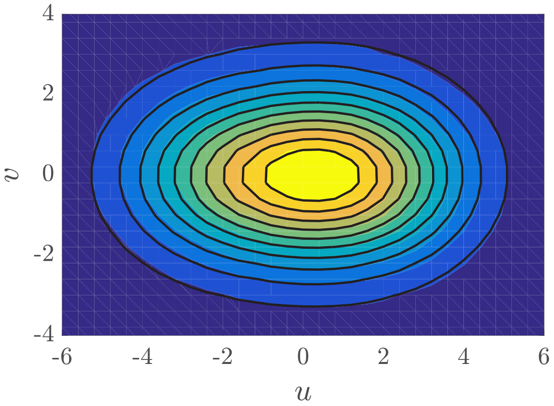

FIG. 4. Color contours are the combined p.d.f. of u and v at a wall-normal height in the logarithmic range, $z^+ = 600$, $z/\delta = 0.06$ in a $Re_\tau \approx 10,000$ boundary layer [24,25]. Cross-wire data are used here. Line contours are the product of the p.d.f. of u and the p.d.f. of v. The contour levels are evenly spaced, and the exact values of the contour levels are not relevant here.

Before we compare the model predictions to data, we make a connection to the random multiplicative process, which has been used to model the energy cascade process in isotropic turbulence (see, e.g., Ref. [33], and the references cited therein). The energy cascade process is a hierarchical process, where turbulent kinetic energy transports from large scales to small scales and lesser scales, until it is dissipated at viscous scales. The random multiplicative models of above process is as follows:

$$\epsilon_l = \prod_{i=1}^{N_l} m_i, \tag{25}$$

where ϵ_l is the instantaneous coarse-grained dissipation rate at the scale l, m_i's are identically, independently distributed random multiplicative, and may be interpreted as the energy transfer rate from a large-scale mother eddy to its next small-scale daughter eddy, the number of multiplicatives depends on the number of cascade steps from the integral scale L to the scale l, and is $N_l \sim \log(L/l)$. If one takes logarithm of Eq. (25), the multiplicative process becomes an additive process, thus presenting to us an exact analogy between the energy cascade in isotropic turbulence and the momentum transport process in wall-bounded flows [1], which is probably already clear from Fig. 1. If the model predictions in this section can be found in data, it would be highly suggestive that a hierarchical structure that exists in the energy cascade process may also exist in the momentum transport process in wall-bounded turbulence.

III. RESULTS

The purpose of this work is to provide empirical support to Eqs. (4) and (5), and the model is validated if the predicted scalings are found in the data. We use cross-wire measurements of boundary layer flows at $\mathrm{Re}_\tau \approx 10\,000$, and compare the data to the predicted scalings in the previous section. We will also provide supporting evidence to a few modeling assumptions, e.g., the assumption of addends b_i's in Eq. (4) and the addends a_i's in Eq. (1) being statistically independent.

A. Statistical independency of the addends contributing to *u* and *v*

Figure 4 shows the combined p.d.f. of the streamwise velocity fluctuation u and the spanwise velocity fluctuation v, $P(u, v)$, at a wall-normal height nominally in the logarithmic region ($z^+ \approx$

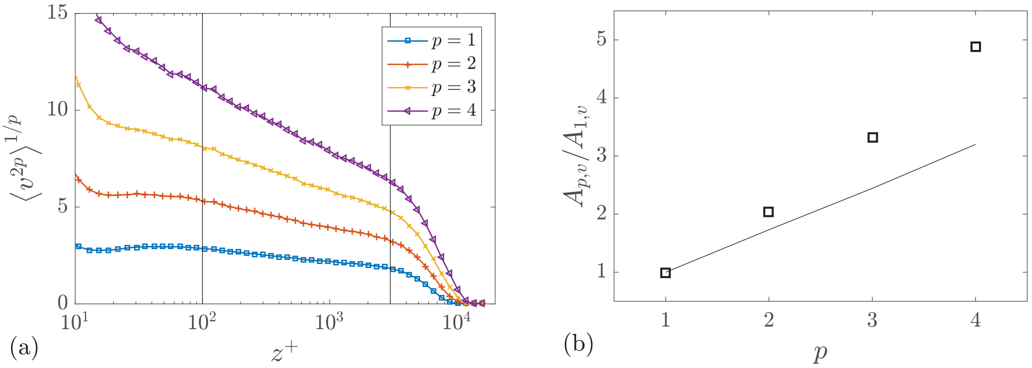

FIG. 5. (a) $\langle v^{2p}\rangle^{1/p}$ as functions of the wall-normal distance for $p = 1, 2, 3, 4$. (b) The measured slope $A_{p,v}/A_{1,v}$ as a function of the moment order p. The solid line corresponds to $[(2p-1)!!]^{1/p}$.

600; $z/\delta \approx 0.06$). The combined p.d.f. is compared to $P(u)\cdot P(v)$ (shown as line contours), where $P(\cdot)$ is the p.d.f. of the bracketed quantity. Figure 4 shows that $P(u, v) \approx P(u)\cdot P(v)$ to a good approximation. Hence, by definition, u and v are statistically independent. The results are the same at other wall-normal distances in the logarithmic range and are not shown here for brevity.

A direct result of the above empirical observation is that the wall-normal velocity fluctuation w, being modeled as proportional to the last addend in u, is also statistically independent of the spanwise velocity component. This leads to trivial scaling predictions including $\langle vw\rangle = 0$, $\langle[v(x) - v(x + r)][w(x) - w(x + r)]\rangle = 0$, etc., which are not discussed in the previous section for brevity.

B. Single-point even-order central moments

Figure 5(a) shows $\langle v^{2p}\rangle^{1/p}$ as functions of the wall-normal distance for $p = 1, 2, 3, 4$ on a semilog scale. A logarithmic scaling is found between $z^+ \approx 100$ and $z/\delta \approx 0.3$. Limited by the statistical convergence, we show only data for $p < 5$. The logarithmic range of $\langle v^2\rangle$ spans more scales than the streamwise counterpart, which is only between $z^+ \approx 3\sqrt{\mathrm{Re}_\tau}$ and $z/\delta \approx 0.15$ [2,34]. The measured slope $A_{1,v} \approx 0.3$ is about 25% smaller than the measurement of 0.4 in a periodic channel at $\mathrm{Re}_\tau \approx 5000$ [32]. This difference in the log-law slopes is notable. Unravelling the physical mechanism behind this difference, however, falls out of the scope of this work and therefore is left for future investigation. Figure 5(b) shows the measured slopes $A_{v,p}$ as a function of p. $A_p - A_{p-1}$ increases as a function of p, and therefore the measurements are super-Gaussian, i.e., $A_{v,p}/A_{v,1} > [(2p-1)!!]^{1/p}$. This is in direct contrast with the streamwise velocity, where previous works have shown that the streamwise velocity statistics are sub-Gaussian [13]. As far as the purpose of this work is concerned, the scalings in Eq. (11) are found, and the data support the HRAP model.

C. Single-point MGFs

Figure 6(a) shows the measured single-point MGFs for a few q values as functions of the wall-normal distance. A power-law scaling is found within the wall-normal distance range $100 \lesssim z^+$, $z/\delta \lesssim 0.3$, i.e., within the same wall-normal distance range where $\langle v_z^2\rangle$ follows a logarithmic scaling. It is worth noting that $\langle\exp(qv)\rangle \neq \langle\exp(-qv)\rangle$ in the near-wall region, leading to a breakdown of the spanwise symmetry. The breakdown in symmetry is thought to arise due to a finite wire separation between the two hot wires in the cross-wire probe. Effects becomes more prominent close to the wall (see the Appendix), leading to a noticeable breakdown in the v symmetry as the probe approaches the wall. In Fig. 6(b), the measured power-law exponent $\tau_v(q)$ is compared to Eq. (10). Furthermore, $\tau_v(q) \geqslant Cq^2$, which is consistent with a super-Gaussian scaling exponent

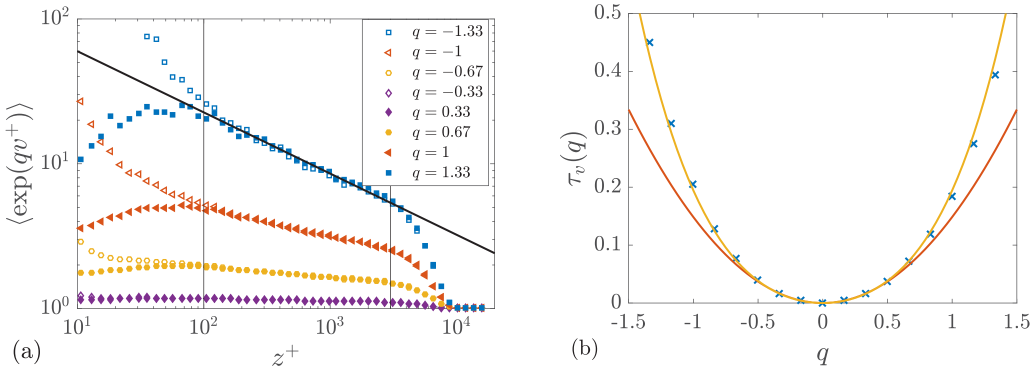

FIG. 6. (a) $\langle\exp(qv)\rangle$ as functions of z for $q = \pm 0.33$, ± 0.67, ± 1.00, ± 1.33. Filled symbols are for positive q's and hollow symbols are used for negative q's. The extent of the power-law scaling is $100 \lesssim z^+$, $z/\delta \lesssim 0.3$, and this range is enclosed within two solid lines. (b) Scaling exponents $\tau_v(q)$ (symbols). A quadratic fit around $q = 0$ leads $\tau_v(q) = 0.15q^2$ (the red solid line). A fourth order polynomial, i.e., $\tau_v(q) = 0.055q^4 + 0.15q^2$ (the yellow solid line), seems to be a good working approximation of the data away from the origin. However, as shown in Eq. (13), only the second order term enters the logarithmic scalings of even order moments.

$\tau_v(q)$. The constant $C \approx 0.15$ [Eq. (10)], leads to $A_{1,v} \approx 0.3$ [Eq. (12)], i.e., the same as the measurement in Sec. III B.

Limited by the data convergence, we have shown data for only $-1.33 \leqslant q \leqslant 1.33$. A larger $|q|$ emphasizes rarer events and therefore is more difficult for statistical convergence. The statistical convergence of a quantity $f(v)$ may be examined using the premultiplied p.d.f., i.e., $f(v) \cdot P(v)$. Figure 7 shows the premultiplied p.d.f. $P(v) \cdot \exp(qv)$ for $q = 1$ and $q = 2$ at a specific wall-normal height $z^+ \approx 600$. The measured $\langle\exp(qv)\rangle$ is the area under the premultiplied p.d.f.. For $q = 1$, the premultiplied p.d.f. drops to ≈ 0 at both ends, and therefore $\langle\exp(v)\rangle$ is statistically converged. For $q = 2$, however, because rare events that contribute to $\langle\exp(2v)\rangle$ do not have a sufficiently large sample, the premultiplied p.d.f. does not drop to 0 at the positive end of v, and therefore $\langle\exp(2v)\rangle$ is not statistically converged. For brevity, this exercise is only done one time for this one quantity. For all other statistics shown in this work, it is implied that the data are statistically converged.

It follows from Eqs. (14) and (15) that the scaling transition is at $\tau_v(q) \approx 0.5$ and $q \approx 1.8$. For this dataset, the data are only statistically converged for $|q| < 1.5$, and therefore the scaling

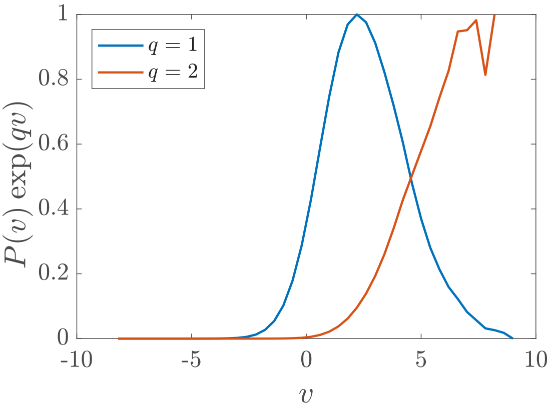

FIG. 7. Premultiplied p.d.f. $P(v) \cdot \exp(qv)$ at $z^+ \approx 600$ for $q = 1, 2$.

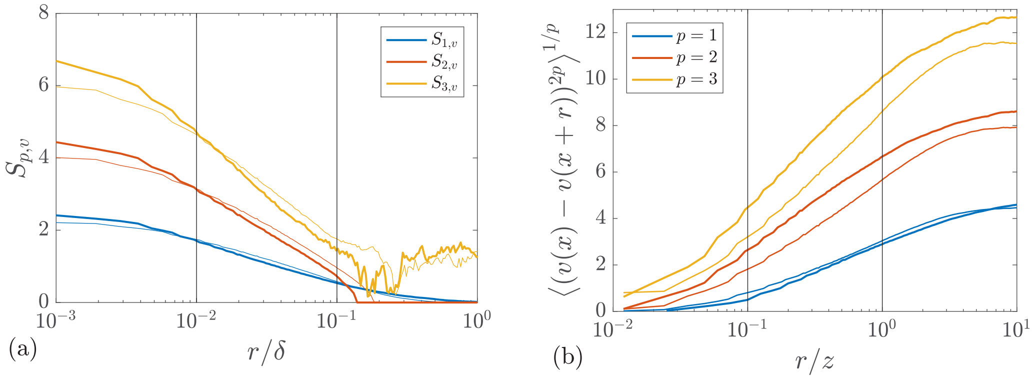

FIG. 8. (a) Linear-log plot of $S_{p,v}$ as functions of r/δ at $z^+ \approx 400$ (bold lines), $z^+ \approx 800$ (thin lines). The extent of the log-law scaling is empirically observed within $0.01 \lesssim r/\delta \lesssim 0.1$, which is marked with the two vertical lines. Panel (b) is the same as (a) but for the streamwise structure functions. The vertical lines enclose the region $0.1 < r/z < 1$.

transition cannot be tested. For brevity, we state without showing evidence that the two-point MGFs follow the expected power-law scalings for $|q| < 1.5$.

D. Spanwise structure functions and generalized two-point correlations

Figure 8(a) shows $S_{p,v}$ [defined in Eqs. (21)] at $z^+ \approx 400$, 800 as functions of the two-point displacement r/δ for $0.001 < r/\delta < 1$. Limited by the data convergence, we only evaluate $S_{p,v}$ for $p \leqslant 3$. Logarithmic scalings are found within $0.01 < r/\delta < 0.1$ for $S_{p,v}$ for $p = 1, 2, 3$. The spanwise structure functions are shown as functions of the two-point displacement in Fig. 8(b), and logarithmic scalings are found within $0.1 \lesssim r/z \lesssim 1$. In conclusion, the scalings in Eqs. (20) and (21) are found, and the data support the HRAP model.

E. Mixed MGFs

We investigate the functional behavior of mixed single-point MGFs. First, a few specific scalings in Eqs. (22) and (24) are compared to the data. Figure 9(a) shows $\langle \exp(qu - qw) \rangle$ as functions of the wall-normal distance. Power-law scalings are found within the wall-normal distance range

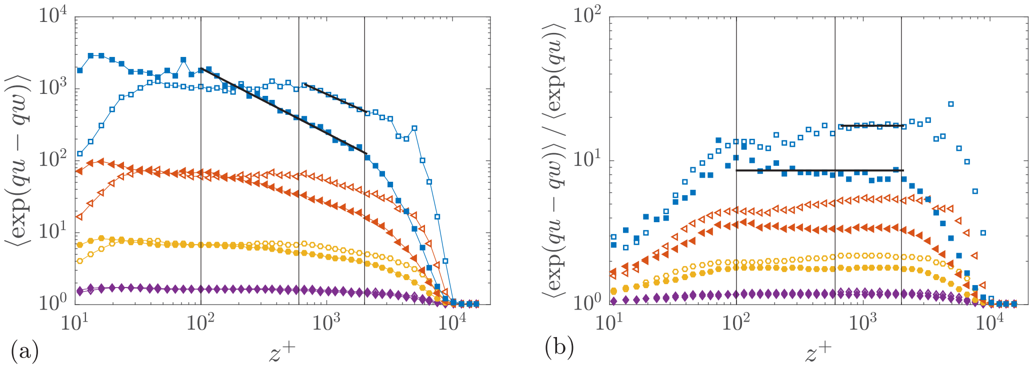

FIG. 9. (a) Log-log plot of $\langle \exp(qu - qw) \rangle$ as functions of z. Symbols are the same as in Fig. 6. The vertical solid lines are at $z^+ = 100$, 600, 2000. The bold solid lines indicates the power-law scalings for $q = \pm 1.33$. (b) Same as (a) but for $\langle \exp(qu - qw) \rangle / \langle \exp(qu) \rangle$.

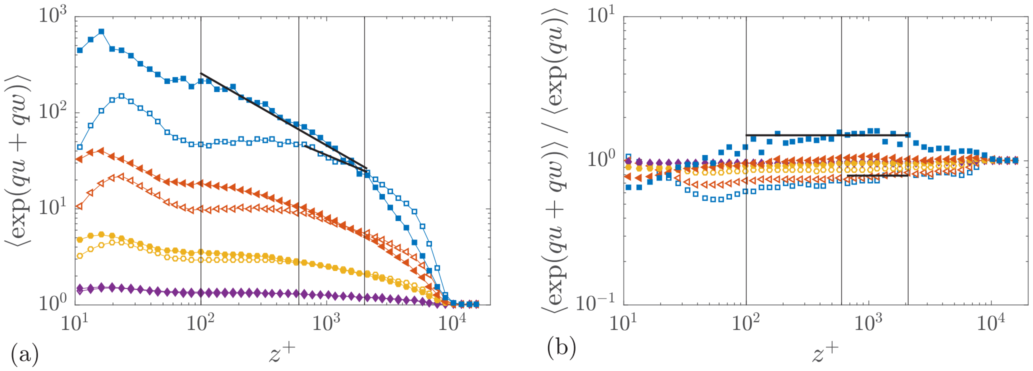

FIG. 10. Same as Fig. 9 but for $q_u = q_w = q$.

$600 \lesssim z^+$, $z/\delta \lesssim 0.2$ for $q < 0$ and $100 \lesssim z^+$, $z/\delta < 0.2$ for $q > 0$. The power-law region is more confined for negative q-valued MGFs than positive q-valued MGFs. The same observation was made in Ref. [17], where the power-law scaling of $\langle\exp(qu)\rangle$ extends more scales for $q > 0$ than for $q < 0$. The HRAP model is a model for flow in the logarithmic range, where fluid motions are dominated by inertia. For a boundary layer at $\mathrm{Re}_\tau \approx 10,000$, the logarithmic range is between $z^+ \approx 400$ and $z/\delta \approx 0.2$. The predicted scaling are found in this region for both positive and negative q values. The fact that the model seems to work still for positive q beyond the logarithmic range may suggest that positive streamwise velocity fluctuations are inertial dominated even below $z^+ \approx 400$. This is possible because positive fluctuations are likely the results of sweep motions, which comes from the upper part of the boundary layer. Figure 9(b) shows $\mathscr{W}(q, -q; z)$ [defined in Eq. (24)] as functions of the wall normal distance. A plateau is found within the wall-normal distance ranges where $\langle\exp(qu - qw)\rangle$ follows a power-law scaling. Figure 10(a) shows $\langle\exp(qu + qw)\rangle$ as functions of the wall-normal distance and Fig. 10(b) shows $\mathscr{W}(q, q; z)$. Power-law scalings are again found. Different from $\mathscr{W}(q, -q; z)$, which is a function of q, $\mathscr{W}(q, q; z)$ is a q-independent constant to a good approximation. As far as this work is concerned, the data are in favor of the HRAP model. A detailed comparison between the measured $\mathscr{W}(q, \pm q; z)$ and the Gaussian approximation are shown in Fig. 11. According to Eq. (24),

$$\mathscr{W}(q, -q; z) = \exp(4C_u q^2), \quad \mathscr{W}(q, q; z) = 1. \tag{26}$$

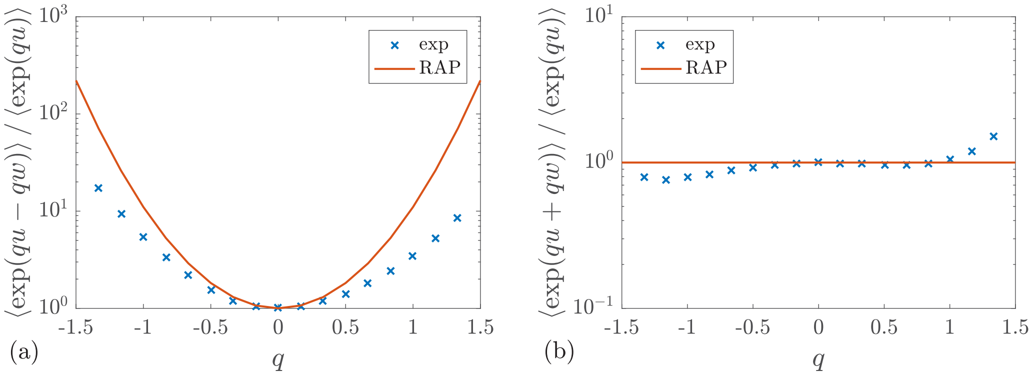

FIG. 11. Measured $\overline{\mathscr{W}(q, \pm q; z)}$ (symbols, denoted as exp) against the model predictions (solid lines, denoted as RAP).

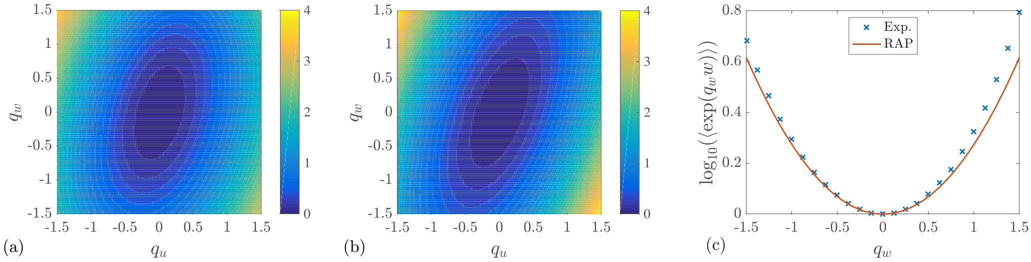

FIG. 12. (a) Measured $\log_{10}(\langle \exp(q_u u + q_w w)\rangle)$ at a fixed wall normal distance $z^+ = 1000$ for q_u, q_w ranging from -1.5 to 1.5. (b) Results from Eq. (22). The prefactor is $C_e = 0.98$. (c) $\log_{10}(\langle \exp(q_u u + q_w w)\rangle)$ at $q_u = 0$.

The constant $C_u = 0.63$ is measured in a previous study [17], and is half of the Townsend-Perry constant A_1. The measurements of $\mathscr{W}(q, \pm q; z)$ in the logarithmic region is

$$\overline{\mathscr{W}(q, \pm q; z)} = \frac{\int \mathscr{W}(q, \pm q; z) d\log(z)}{\int d\log(z)}, \tag{27}$$

where the integration is $100 < z^+$, $z/\delta < 0.2$ for $q < 0$ and $600 < z^+$, $z/\delta < 0.2$ for $q > 0$. The integration is based on $d\log(z)$ instead of z to give equal weights to attached eddies of different scales. For $\mathscr{W}(q, -q; z)$, the data are sub-Gaussian. For $\mathscr{W}(q, q; z)$, the data deviate slightly from unit at large $|q|$.

Last, we study the functional behavior of MGF $\langle \exp(q_u u + q_w w)\rangle$. We measure $\langle \exp(q_u u + q_w w)\rangle$ at $z^+ \approx 1000$ (a height corresponds to $z/\delta = 0.1$) for q_u, q_w ranging from -1.5 to 1.5. The measurements are shown in Fig. 12(a). Figure 12(b) corresponds to Eq. (23). A constant C_e is used such that the difference between $\log_{10}(C_e(z/\delta)^{-C_u q_u^2} e^{C_u (q_u - q_w)^2})$ and the measured $\log_{10}(\langle \exp(q_u u + q_w w)\rangle)$ is minimum in an $L2$ sense. Furthermore, it is worth noting that we encountered difficulties when trying to directly evaluate $\log_{10}(C_e(z/\delta)^{-C_u q_u^2} e^{C_u (q_u - q_w)^2})$, presumably due to insufficient numerical precision. Instead, here we evaluate $-C_u q_u^2 \log_{10}(C_e(z/\delta)) + C_u (q_u - q_w)^2 \log_{10}(e)$, which is analytically equivalent. According to Fig. 12(a), events in the first and third quadrants dominate [35]. Comparing Figs. 12(a) and 12(b), Gaussianity leads to stronger stretching in the direction of w. Figure 12(c) shows the measured and the modeled $\langle \exp(qw)\rangle$ [i.e., slices along $u = 0$ of Figs. 12(a) and 12(b)] at $z^+ = 1000$, where it is evident that the Gaussian model under-predicts the empirical results. The fact that the Gaussianity leads to stronger stretching than the measurements in Fig. 12, suggests that the wall-normal velocity is super-Gaussian. A similar observation was made in Ref. [36], where super-Gaussianity was also found in the wall-normal component. Except for the stretching in the q_w axis, the model otherwise agrees well with the data. The results at other wall-normal planes are very similar and are not shown here for brevity.

IV. CONCLUSIONS

The HRAP model is extended to account for the spanwise and the wall normal velocity fluctuations in the logarithmic region. Following the HRAP model to its logic conclusions, we have provided scaling predictions for a few different flow statistics that involve v, and such statistics include the single-point, two-point moment generating functions, streamwise structure function, generalized two-point correlations, and mixed single-point MGFs. Empirical evidence for these scalings is shown, and the data generally support the HRAP model. Measurements show that $\langle \exp(qv)\rangle \sim (\delta/z)^{0.055q^4+0.15q^2}$, $\exp(qw) \sim \exp(0.63q^2)$ (cf. Figs. 6 and 12). The proportional constants are left undetermined as they depends on the flow and are not universal. The constant $C_u = 0.63$ corresponds to half of the Townsend-Perry constant $A_1/2$. The constant 0.15 is half of spanwise counterpart of the Townsend-Perry constant, i.e., the slope of the logarithmic scaling of $\langle v^2 \rangle$. The streamwise moment generating function was already measured in Ref. [17]. The above formulations can be used to determine the scaling of the central moments and the slope of the resulting logarithmic scalings. The intercepts of these logarithmic scalings, however, depends on the proportional constants in the above formulations and are not universal. In this work, we have examined moments up to the sixth order. Converged statistics of higher order moments will require more data and will be examined in future works. As the HRAP model can already account for the streamwise velocity fluctuation [6], by accounting for both the spanwise and the wall-normal velocity fluctuations, the model provides a complete description of velocity fluctuations in all three Cartesian directions in the logarithmic region. It is worth noting that we have put our emphasis on identifying and verifying the forms of the predicted scalings, not the constants in them, which is by itself an interesting topic that worth investigating in the future.

Although HRAP itself does predict the exact values of the constants in the various scalings, it is worth noting that the model as is can already be used for predictive modeling. For example, in LES wall modeling, if one needs information about u^2 in the first cell, where the eddies are not resolved, one could adopt the logarithmic scaling $u^2 \sim \log(z)$, and use a dynamic procedure to determine the coefficients from the resolved motions.

The obtained new physical insights may also be incorporated into wall-modeled turbulence simulations. For this, it is necessary to make use of numerical methods that easily encapsulate the high-order moment information of near-wall flow fields. The recently popularized discontinuous Galerkin method [37–39] based on variational formulation could be a good candidate.

ACKNOWLEDGMENTS

X.Y. thanks C. Meneveau and P. Johnson for fruitful discussion. I.M. and R.B. acknowledge the financial support of the Australian Research Council.

APPENDIX: EFFECTS OF VERTICAL DISPLACEMENT OF HOT WIRES IN A CROSS-WIRE PROBE

Because of the symmetry in the spanwise direction, one expects $\langle \exp(qv) \rangle = \langle \exp(-qv) \rangle$. This expectation bears out for $z^+ \gtrsim 200$, but for $z^+ \lesssim 200$, negative-q-valued MGFs are consistently higher than positive-q-valued MGFs (see Fig. 6). This asymmetry is highlighted in the p.d.f. of the spanwise velocity fluctuation (shown in Fig. 13), where the p.d.f. of v is shown as functions of both v^+ and $-v^+$. The asymmetry is likely due to the finite displacement of the two hot wires (in

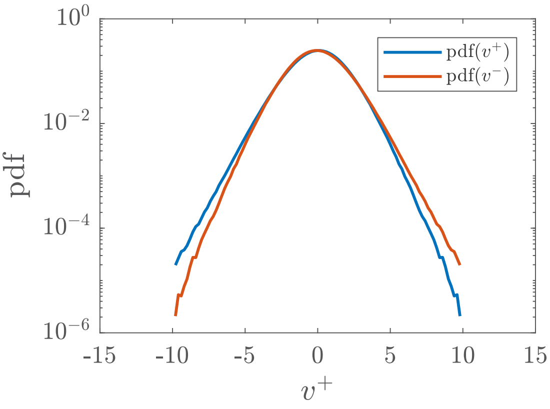

FIG. 13. The p.d.f. of the spanwise velocity v at $z^+ = 42$. The p.d.f.'s are shown as functions of both v^+ and $-v^+$ to emphasize the asymmetry in the measurements.

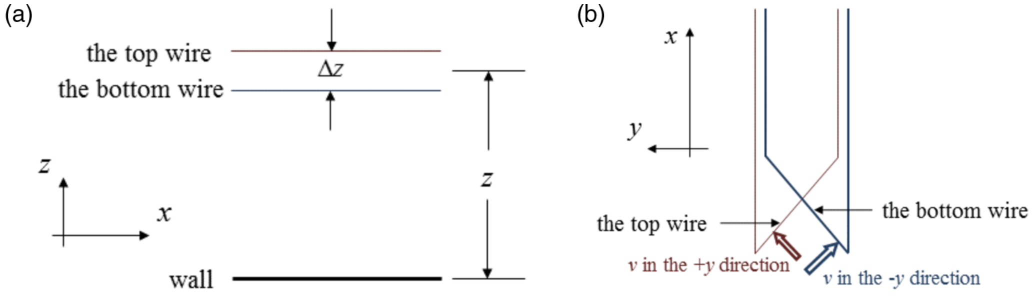

FIG. 14. A sketch of the setup of a cross wire that measures both the streamwise and the spanwise velocities. The cross wire is placed at a wall normal distance z. The two wires are displaced by a small distance Δz (to prevent a short circuit). (a) Side view. (b) Top view.

a cross wire) in the wall-normal direction (see Fig. 14 for a sketch of the wire setup). Because of this setup, measurements of the spanwise velocity in the positive-y direction and in the negative-y directions are not at the same wall-normal height, leading to the observed asymmetry in Fig. 13. As sketched in Fig. 14, the top wire is more sensitive to v fluctuations in the positive-y direction and the bottom wire to v fluctuations in the negative-y direction. While the effect of the displacement Δz is negligible for $z \gg \Delta z$, this displacement becomes significant for measurements in the near wall region.

To quantify the effect of the above mentioned misplacement on $\langle \exp(|q|v)\rangle$, $\langle \exp(-|q|v)\rangle$, we use the following quantity

$$\rho_a = \frac{\langle \exp(qv)|v > 0\rangle}{\langle \exp(-qv)|v < 0\rangle}.$$

Without loss of generality, we take $q > 0$. Because $\langle \exp(qv)\rangle \sim (z/\delta)^{-\tau_v(q)}$, ρ_a is approximately

$$\rho_a = \left(\frac{z - \Delta z/2}{z + \Delta z/2}\right)^{-\tau_v(q)}. \tag{A1}$$

The displacement Δz is constant for a given cross wire. For a fixed q, ρ_a is 1 for large z values; for a fixed z, ρ_a deviates from unit as q increases, leading to the observed asymmetry in Fig. 6. The distance between the two wires is 2 mm. We compare Eq. (A1) to data in Fig. 15. The comparison

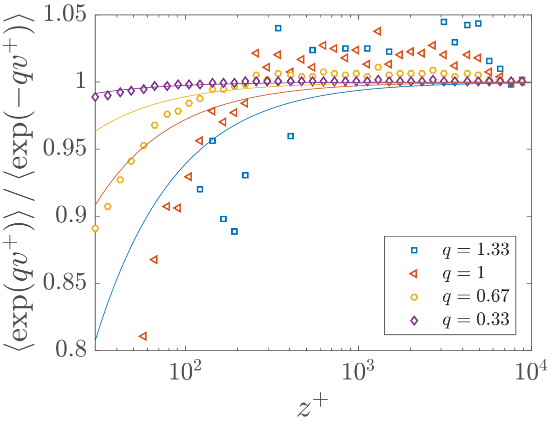

FIG. 15. A comparison of the measured $\langle \exp(qv)\rangle / \langle \exp(-qv)\rangle$ to Eq. (A1).

is only meaningful in the wall-normal distance range where a power law scaling of $\langle \exp(qv) \rangle$ is expected. The data is not inconsistent with our interpretation.

It is worth noting that this asymmetry is not because of the finite span of the hot wire. Finite span of a hot wire leads to spatially filtering of the velocity signal [40,41], and can be highlighted using conventional central moments.

[1] J. Jiménez, Cascades in wall-bounded turbulence, Ann. Rev. Fluid Mech. **44**, 27 (2011).

[2] I. Marusic, J. P. Monty, M. Hultmark, and A. J. Smits, On the logarithmic region in wall turbulence, J. Fluid Mech. **716**, R3 (2013).

[3] A. Perry and M. Chong, On the mechanism of wall turbulence, J. Fluid Mech. **119**, 173 (1982).

[4] J. Bretheim, C. Meneveau, and D. F. Gayme, Standard logarithmic mean velocity distribution in a band-limited restricted nonlinear model of turbulent flow in a half-channel, Phys. Fluids **27**, 011702 (2015).

[5] J. Woodcock and I. Marusic, The statistical behavior of attached eddies, Phys. Fluids **27**, 015104 (2015).

[6] X. I. A. Yang, I. Marusic, and C. Meneveau, Hierarchical random additive process and logarithmic scaling of generalized high order, two-point correlations in turbulent boundary layer flow, Phys. Rev. Fluids **1**, 024402 (2016).

[7] A. Townsend, *The Structure of Turbulent Shear Flow* (Cambridge University Press, Cambridge, 1976).

[8] A. Perry, S. Henbest, and M. Chong, A theoretical and experimental study of wall turbulence, J. Fluid Mech. **165**, 163 (1986).

[9] A. E. Perry and I. Marusic, A wall-wake model for the turbulence structure of boundary layers. Part 1. Extension of the attached eddy hypothesis, J. Fluid Mech. **298**, 361 (1995).

[10] I. Marusic and A. E. Perry, A wall-wake model for the turbulence structure of boundary layers. Part 2. Further experimental support, J. Fluid Mech. **298**, 389 (1995).

[11] C. M. de Silva, J. D. Woodcock, N. Hutchins, and I. Marusic, Influence of spatial exclusion on the statistical behavior of attached eddies, Phys. Rev. Fluids **1**, 022401 (2016).

[12] I. Marusic and J. P. Monty, Attached eddy model of wall turbulence, Ann. Rev. Fluid Mech. (2019).

[13] C. Meneveau and I. Marusic, Generalized logarithmic law for high-order moments in turbulent boundary layers, J. Fluid Mech. **719**, R1 (2013).

[14] C. M. de Silva, I. Marusic, J. D. Woodcock, and C. Meneveau, Scaling of second- and higher-order structure functions in turbulent boundary layers, J. Fluid Mech. **769**, 654 (2015).

[15] U. Frisch, Fully developed turbulence and intermittency, Ann. N.Y. Acad. Sci. **357**, 359 (1980).

[16] Z.-S. She and E. Leveque, Universal Scaling Laws in Fully Developed Turbulence, Phys. Rev. Lett. **72**, 336 (1994).

[17] X. I. A. Yang, I. Marusic, and C. Meneveau, Moment generating functions and scaling laws in the inertial layer of turbulent wall-bounded flows, J. Fluid Mech. **791**, R2 (2016).

[18] X. I. A. Yang, R. Baidya, P. Johnson, I. Marusic, and C. Meneveau, Structure function tensor scaling in the logarithmic region derived from the attached eddy model of wall-bounded turbulent flows, Phys. Rev. Fluids **2**, 064602 (2017).

[19] X. I. A. Yang and A. Lozano-Durán, A multifractal model for the momentum transfer process in wall-bounded flows, J. Fluid Mech. **824**, R2 (2017).

[20] J. C. Del Alamo, J. Jiménez, P. Zandonade, and R. D. Moser, Scaling of the energy spectra of turbulent channels, J. Fluid Mech. **500**, 135 (2004).

[21] D. Krug, X. I. A. Yang, C. M. de Silva, R. Ostilla-Mónico, R. Verzicco, I. Marusic, and D. Lohse, Statistics of turbulence in the energy-containing range of Taylor–Couette compared to canonical wall-bounded flows, J. Fluid Mech. **830**, 797 (2017).

[22] J. A. Sillero, J. Jiménez, and R. D. Moser, Two-point statistics for turbulent boundary layers and channels at Reynolds numbers up to $\delta^+ \approx 2000$, Phys. Fluids **26**, 105109 (2014).

[23] C. M. de Silva, K. Kevin, R. Baidya, N. Hutchins, and I. Marusic, Large coherence of spanwise velocity in turbulent boundary layers, J. Fluid Mech. **847**, 161 (2018).

[24] R. Baidya, *Multicomponent Velocity Measurements in Turbulent Boundary Layers*, Ph.D. thesis, University of Melbourne (2016).

[25] J. Philip, R. Baidya, N. Hutchins, J. P. Monty, and I. Marusic, Spatial averaging of streamwise and spanwise velocity measurements in wall-bounded turbulence using V- and ×-probes, Meas. Sci. Technol. **24**, 115302 (2013).

[26] E. Hopf, Statistical hydromechanics and functional calculus, J. Ration. Mech. Anal. **1**, 87 (1952).

[27] A. S. Monin and A. M. Yaglom, *Statistical Fluid Mechanics, Vol. II: Mechanics of Turbulence* (Courier Corporation, Chelmsford, MA, 2013).

[28] X. I. A. Yang, C. Meneveau, I. Marusic, and L. Biferale, Extended self-similarity in moment-generating-functions in wall-bounded turbulence at high reynolds number, Phys. Rev. Fluids **1**, 044405 (2016).

[29] M. K. Simon, *Probability Distributions Involving Gaussian Random Variables: A Handbook for Engineers and Scientists* (Springer Science & Business Media, Berlin, 2007).

[30] K. M. Talluru, R. Baidya, N. Hutchins, and I. Marusic, Amplitude modulation of all three velocity components in turbulent boundary layers, J. Fluid Mech. **746**, R1 (2014).

[31] M. Bernardini, S. Pirozzoli, and P. Orlandi, Velocity statistics in turbulent channel flow up to $\mathrm{Re}_\tau = 4000$, J. Fluid Mech. **742**, 171 (2014).

[32] M. Lee and R. D. Moser, Direct numerical simulation of turbulent channel flow up to $\mathrm{Re}_\tau \approx 5200$, J. Fluid Mech. **774**, 395 (2015).

[33] U. Frisch, *Turbulence: The Legacy of A. N. Kolmogorov* (Cambridge University Press, Cambridge, 1995).

[34] M. Hultmark, M. Vallikivi, S. C. C. Bailey, and A. J. Smits, Turbulent Pipe Flow at Extreme Reynolds Numbers, Phys. Rev. Lett. **108**, 094501 (2012).

[35] J. M. Wallace, Quadrant analysis in turbulence research: History and evolution, Ann. Rev. Fluid Mech. **48**, 131 (2016).

[36] H. Fernholz, E. Krause, M. Nockemann, and M. Schober, Comparative measurements in the canonical boundary layer at $\mathrm{Re}_{\delta_2} \leqslant 6 \times 10^4$ on the wall of the German–Dutch windtunnel, Phys. Fluids **7**, 1275 (1995).

[37] Z. J. Wang, K. Fidkowski, R. Abgrall, F. Bassi, D. Caraeni, A. Cary, H. Deconinck, R. Hartmann, K. Hillewaert, H. T. Huynh, N. Kroll, G. May, P.-O. Persson, B. van Leer, and M. Visbal, High-order CFD methods: Current status and perspective, Int. J. Numer. Methods Fluids **72**, 811 (2013).

[38] K. Hillewaert, J. S. Cagnone, S. M. Murman, A. Garai, Y. Lv, and M. Ihme, Assessment of high-order DG methods for LES of compressible flows, in *Proceedings of the Summer Program, Center for Turbulence Research, Stanford University* (2016), p. 363.

[39] Y. Lv, P. C. Ma, and M. Ihme, On underresolved simulations of compressible turbulence using an entropy-bounded DG method: Solution stabilization, scheme optimization, and benchmark against a finite-volume solver, Computers & Fluids **161**, 89 (2018).

[40] N. Hutchins, T. B. Nickels, I. Marusic, and M. Chong, Hot-wire spatial resolution issues in wall-bounded turbulence, J. Fluid Mech. **635**, 103 (2009).

[41] P. Ligrani and P. Bradshaw, Spatial resolution and measurement of turbulence in the viscous sublayer using subminiature hot-wire probes, Exp. Fluids **5**, 407 (1987).